First-principles interatomic potentials for transition-metal aluminides: Theory and trends across the 3*d* series

John A. Moriarty
Lawrence Livermore National Laboratory, University of California, Livermore, California 94551

Mike Widom
Department of Physics, Carnegie Mellon University, Pittsburgh, Pennsylvania 15213
(Received 17 April 1997)

In this paper the first-principles generalized pseudopotential theory (GPT) of transition-metal interatomic potentials [J. A. Moriarty, Phys. Rev. B **38**, 3199 (1988)] is extended to *AB* binary compounds and alloys. For general transition-metal (TM) systems, the GPT total-energy functional involves a volume term, central-force pair potentials, and angular-force multi-ion potentials, which are both volume (Ω) and concentration (x) dependent and include all *sp*, *sp-d*, and *d-d* interactions within local density-functional quantum mechanics. The formalism is developed here in detail for intermetallic systems where *A* is a simple metal and *B* is a transition metal and applied to the prominent special case of the transition-metal aluminides TM_xAl_{1-x}, where *sp-d* hybridization is especially important. Emphasis is given to the aluminum-rich 3*d* binary systems for $x<0.30$, which appear to be well described at the pair-potential level without angular forces and for which the present GPT potentials can be used directly in atomistic simulations. Volume terms and pair potentials for all of the 3*d* aluminides have been calculated and their behavior with atomic number, Ω, and x is elaborated through illustrative applications to the cohesive and structural trends across the 3*d* series. More extensive applications to the Co-Al and Ni-Al phase diagrams will be given elsewhere. [S0163-1829(97)03938-6]

I. INTRODUCTION

For *sp*-bonded compounds and alloys, the fundamental theory of bulk interatomic potentials has been well developed from rigorous plane-wave pseudopotential expansions and successfully applied to obtain both solid and liquid properties, including the structural phase diagrams of simple-metal intermetallic systems.[1] A corresponding first-principles theory for *d*- and *sp-d*-bonded transition-metal intermetallics has heretofore been lacking, although there have been encouraging successes with simplified semiempirical approaches, especially for the structurally complex transition-metal (TM) aluminides.[2,3] In addition, a number of important aspects of structural phase stability in TM aluminide compounds and alloys have been illuminated recently via *ab initio* electronic-structure calculations[4–8] within the local-density approximation (LDA) of density-functional theory.[9] At the same time, the essential groundwork has been laid for an *ab initio* approach to interatomic potentials in TM intermetallics with the development of generalized pseudopotential theory (GPT), which provides a fundamental basis for such potentials in elemental simple and transition metals within the same LDA framework.[10–12] The purpose of this paper is to extend the GPT to *AB* binary transition-metal systems, with an emphasis on obtaining first-principles interatomic potentials for the TM aluminides.

In the GPT a mixed basis set of plane waves and localized *d* states is used to expand the electron density and total energy of a TM system in terms of weak *sp* pseudopotential, *sp-d* hybridization, and *d-d* tight-binding matrix elements. In a real-space formulation, the derived interatomic potentials become well-defined functionals of these matrix elements and all quantities may be evaluated directly from first principles without any external input. For an elemental bulk transition metal, the GPT provides a rigorous expansion of the total energy in the form[12]

$$E_{\rm tot}(\mathbf{R}_1,\ldots,\mathbf{R}_N)=NE_{\rm vol}(\Omega)+\frac{1}{2}{\sum_{i,j}}' v_2(ij)+\frac{1}{6}{\sum_{i,j,k}}' v_3(ijk)+\frac{1}{24}{\sum_{i,j,k,l}}' v_4(ijkl), \tag{1}$$

where $\mathbf{R}_1,\ldots,\mathbf{R}_N$ denotes the positions on the N ions in the metal, Ω is the atomic volume, and the prime on each sum over ion positions excludes all self-interaction terms where two indices are equal. The leading volume term in this expansion $E_{\rm vol}$ as well as the two-, three-, and four-ion interatomic potentials v_2, v_3, and v_4 are volume dependent but *structure independent* quantities and thus *transferable* to all bulk ion configurations. At constant volume Ω, the radial-force pair potential v_2 is a one-dimensional function of the ion-ion separation distance $R_{ij}=|\mathbf{R}_i-\mathbf{R}_j|$:

$$v_2(ij)=v_2(R_{ij};\Omega), \tag{2}$$

while the angular-force triplet potential v_3 and quadruplet potential v_4 are, respectively, the three- and six-dimensional functions

$$v_3(ijk)=v_3(R_{ij},R_{jk},R_{ki};\Omega) \tag{3}$$

and

$$v_4(ijkl)=v_4(R_{ij},R_{jk},R_{kl},R_{li},R_{ki},R_{lj};\Omega). \quad (4)$$

The nature of these functionals is complex and reflects the material-dependent electronic band structure of the metal including the effects of partial d-band filling and self-consistent electron screening. Detailed expressions and calculated results for the $3d$ and $4d$ transition metals are given in Ref. 12. As in the case of sp-bonded simple metals, where angular forces become unimportant, the sp pseudopotential contributions to the total energy are retained only to the pair-potential level, i.e., for $E_{\rm vol}$ and v_2. Thus the multi-ion potentials v_3 and v_4 reflect sp-d hybridization and d-d tight-binding contributions and the angular forces for transition metals are a direct result of these d-state interactions. In general, both the pair potential v_2 and the multi-ion potentials v_3 and v_4 are long ranged with aysmptotic Friedel-like oscillations arising from sp-d hybridization as well as electron screening. The sign and amplitude of the potentials at short range, on the other hand, strongly reflect d-band filling, with typically v_2 attractive, v_3 repulsive, and v_4 oscillatory.

The transition-metal GPT formalism readily folds down into simpler forms in the special cases of completely empty or filled d bands encountered in pre- and post-transition metals.[10,11] This includes the limiting simple-metal case appropriate to aluminum. In the transition-metal limit, self-consistent electron-density constraints establish the balance between the sp-band occupation per atom or valence Z and the d-band occupation per atom Z_d, resulting in partial d-band filling and the multi-ion d-state interactions. In the simple-metal limit, on the other hand, Z is fixed by the chemical valence of the element in question, $Z_d \to 0$ or 10 as appropriate, and the sp-d hybridization and d-d tight-binding interactions become negligible. Any remaining d-state contributions are absorbed into the nonlocal pseudopotential, and the simple-metal GPT, which is carried to the level of v_2 in Eq. (1), becomes a refined version of the conventional plane-wave pseudopotential perturbation theory.[1]

For transition-metal compounds and alloys, one may readily anticipate the broad features a multicomponent extension of the GPT must accommodate. We specifically consider an AB binary system with concentrations $c_A=N_A/N$ of A metal atoms and $c_B=N_B/N$ of B metal atoms and introduce the single concentration variable

$$x \equiv c_B = 1-c_A. \quad (5)$$

From general considerations, one can expect that both the volume term and the interatomic potentials in Eq. (1) will become concentration dependent as well as volume dependent. Thus, for example,

$$E_{\rm vol}(\Omega) \to E_{\rm vol}(\Omega,x) \quad (6)$$

in a binary intermetallic system, with Ω and x as independent variables. The appropriate multiplicity of interatomic potentials must also be accommodated, so that in general there are three independent two-ion pair potentials

$$v_2 \to v_2^{AA}, v_2^{AB}, v_2^{BB}, \quad (7)$$

four independent three-ion triplet potentials

$$v_3 \to v_3^{AAA}, v_3^{AAB}, v_3^{ABB}, v_3^{BBB}, \quad (8)$$

and five independent four-ion quadruplet potentials

$$v_4 \to v_4^{AAAA}, v_4^{AAAB}, v_4^{AABB}, v_4^{ABBB}, v_4^{BBBB}. \quad (9)$$

In addition, self-consistent electron-density constraints must now be satisfied, which link the sp valences Z_A and Z_B with the d-band occupations Z_d^A and Z_d^B as functions of both volume and concentration. The general case is consequently quite complicated and requires the complete specification of two sets of localized d states for the two constituents and the calculation of all appropriate d-d cross terms. While there is no difficulty in setting up the formalism for this case, as yet the corresponding computational capability does not exist. We shall therefore narrow our focus to the formally simpler case of an AB intermetallic system where the A component is a simple metal, with fixed Z_A and Z_d^A, and the B component is a transition metal, with variable Z_B and Z_d^B. In the spirit of the elemental GPT, we retain only the pair potentials v_2^{AA}, v_2^{AB}, and v_2^{BB} and the multi-ion potentials v_3^{BBB} and v_4^{BBBB} in this case. Moreover, we may anticipate that for sufficiently small x the latter remaining multi-ion potentials will also be negligible and a good description of the system can be obtained at the pair-potential level without angular forces.

The prototype systems to which the present formalism applies are the transition-metal aluminides TM_xAl_{1-x}. The aluminides are both of technological interest as high-temperature structural materials with desirable mechanical properties and of basic scientific interest because of the complex phases these materials form and their intimate connection to quasicrystals. With regard to mechanical properties, LDA electronic-structure methods have been applied to $B2$ compounds to calculate the elastic moduli of CoAl (Ref. 13) and point-defect properties of FeAl and NiAl,[14] while empirical embedded-atom-method (EAM) potentials have been used for more general studies of defects in Ti-Al and Ni-Al compounds, including calculations of vacancies, grain boundaries, and dislocations.[15–17] With regard to complex phases, semiempirical pair potentials, based on model pseudopotential and hybridization interactions, have helped to explain the appearance of some of these phases in aluminum-rich systems,[2,3] while semiempirical tight-binding (TB) potentials have been used to study the structure of corresponding liquid alloys.[18] Unlike the EAM and TB potentials, however, the pair potentials contain the expected long-ranged oscillatory tails, which are really essential to account for the complex aluminide phases in the solid.

The semiempirical aluminide pair potentials[2,3] are also qualitatively similar to the present GPT pair potentials and may be viewed as a highly simplified version of the latter. The former potentials were most completely developed by Phillips *et al.*[3] in the case of Co-Al for application to the aluminum-rich phase diagram. These potentials are based on a two-parameter local pseudopotential treatment of the sp interactions and a three-parameter model Hamiltonian treatment of the sp-d hybridization that neglects nonorthogonality effects. No attempt was made, however, to treat direct d-d interactions, the volume and concentration dependence of the potentials, nor self-consistent electron screening. In contrast, the present first-principles GPT explicitly includes the additional features of nonlocal pseudopotentials and di-

rect d-d interactions, as well as full treatments of sp-d hybridization, self-consistent electron screening, and the volume and concentration dependence of the total energy. We expect, therefore, that a wide variety of aluminide properties can eventually be treated with the GPT, including defects, structural phase stability, lattice vibrations, melting, and liquid structure. More generally, the GPT pair potentials should be readily applicable to both static and dynamic simulations of materials properties.

The outline of this paper is as follows. In Sec. II we first establish the self-consistent electron-density constraints that must be satisfied by our AB intermetallic system and apply these conditions to the $3d$ aluminides. Next in Sec. III we outline the formalism for the GPT interatomic potentials and use this formalism to calculate $3d$ aluminide potentials as a function of atomic number, volume, and concentration. Then in Sec. IV we use the calculated potentials to address the basic cohesive and structural trends across the $3d$ series and thereby demonstrate the promise of the GPT for aluminide phase diagrams. We conclude in Sec. V, with additional technical details on the GPT formalism given in the Appendix.

II. SELF-CONSISTENT ELECTRON-DENSITY CONSTRAINTS

To extend the GPT formalism to binary intermetallics, one must first ensure that the basic conditions of electron-density continuity are satisfied. For a given average atomic volume Ω, the zeroth-order sp electron density of the system is Z/Ω, where Z is the concentration-weighted average

$$Z = c_A Z_A + c_B Z_B = (1-x) Z_A + x Z_B , \tag{10}$$

with Z_A and Z_B the respective sp valences of the A and B components. It is also useful to define individual atomic volumes Ω_A and Ω_B such that

$$\Omega = c_A \Omega_A + c_B \Omega_B = (1-x)\Omega_A + x\Omega_B \tag{11}$$

and

$$Z/\Omega = Z_A/\Omega_A = Z_B/\Omega_B . \tag{12}$$

In analogy with the elemental GPT, the parameter pairs Z_A, Ω_A and Z_B, Ω_B define zeroth-order pseudoatoms for the A and B components, respectively. These pseudoatoms are self-consistent A- and B-metal ions that have been neutralized by the common uniform electron gas and establish properly shifted inner-core and d-state energy levels and corresponding basis functions that are needed in the full GPT formalism. Physically, one may think of the A- and B-metal pseudoatoms as being expanded or contracted from their elemental bulk sizes to ensure that Eq. (12) is satisfied. For nontransition-metal systems, where Z_A and Z_B are fixed quantities, it is, of course, a simple matter to satisfy Eqs. (10)–(12) directly. In transition-metal systems, on the other hand, where Z_A and/or Z_B are volume and concentration dependent, the situation is considerably more complex. For the case of primary interest in this paper, where A is a simple metal and B is a transition metal, one must simultaneously satisfy the equilibrium conditions between the sp valence Z_B and d-electron occupation number Z_d^B for the B-metal component, as given by Eqs. (66)–(68) of Ref. 12. These conditions link Z_B and Z_d^B through the Fermi level ϵ_F and the $\ell = 2$ phase shift δ_2 associated with the B site and can be written

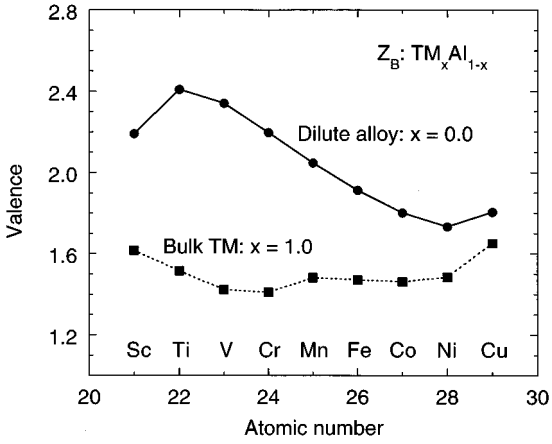

FIG. 1. Transition-metal valence Z_B for the $3d$ aluminides TM_xAl_{1-x} in the $x=1$ and $x=0$ concentration limits.

$$Z_d^B = \frac{10}{\pi}\delta_2(\epsilon_F), \tag{13}$$

$$\epsilon_F = \frac{\hbar^2}{2m}\left(\frac{3\pi^2 Z}{\Omega}\right)^{2/3}, \tag{14}$$

which can also be expressed in the familiar form $Z = k_F^3 \Omega/3\pi^2$, where k_F is the corresponding Fermi wave number, and

$$Z_B + Z_d^B = Z_a^B - Z_c^B , \tag{15}$$

where Z_a^B is the atomic number and Z_c^B is the number of inner-core electrons of the B-metal ion. The Fermi energy ϵ_F and the phase shift δ_2 both depend on the intermetallic environment, so Z_B and Z_d^B will be shifted away from their bulk values. For given values of Ω, x and Z_A, Eqs. (10)–(15) represent seven equations in seven unknowns and must be iterated numerically, via the A- and B-metal pseudoatoms, to achieve a self-consistent solution. An efficient strategy to accomplish this is discussed in the Appendix, together with technical details on how the pseudoatom calculation is modified in the binary intermetallic case. The primary modification concerns the common location of the zero of energy at the valence-band minimum, which becomes concentration dependent in the alloy. We also now use the very accurate exchange-correlation parametrization of Vosko *et al.*[19] in place of the Hedin-Lundqvist parametrization[20] used in Refs. 10–12.

Figures 1 and 2 illustrate the calculated changes in Z_B and Ω_B, respectively, for the $3d$ TM aluminides in going from the bulk transition-metal $x=1$ limit to the aluminum-rich dilute-alloy $x=0$ limit. These results have been obtained at the observed equilibrium volumes ($\Omega = \Omega_0$) of the $3d$ metals for $x=1$ and of Al for $x=0$. Quantitative values are listed in Table I and calculational details are discussed in the Appendix. In the bulk transition metals, $Z_B \approx 1.5$ across the $3d$ series. Bulk aluminum, on the other hand, with $Z_A = 3$ has a

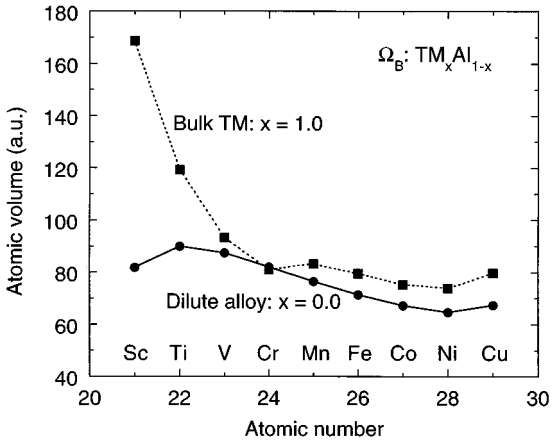

FIG. 2. Transition-metal atomic volume Ω_B for the $3d$ aluminides TM_xAl_{1-x} in the $x=1$ and $x=0$ concentration limits.

considerably higher sp electron density than any of the transition metals. When a transition metal is added to aluminum, therefore, we expect Z_B to rise and/or Ω_B to decrease in order to create a higher density. As shown in Figs. 1 and 2, both of these changes actually occur at $x=0$, with the biggest quantitative impact on the left-hand side of the $3d$ series where $Z_B>2$ for Sc through Mn and Ω_B is dramatically reduced for Sc and Ti. More generally, the increase in Z_B in the TM aluminides is balanced by a corresponding decrease in Z_d^B, which in turn is provided by the TM d bands rising in energy, broadening, and unfilling in the alloy.

While the volume Ω and concentration x are independent variables, there is, of course, a high correlation between x and the *equilibrium* volume Ω_0 observed in alloys and compounds. Approximate relations linking Ω_0 and x are often useful for preliminary calculations or in cases where data on particular phases do not exist. We mention here one such relation that is appropriate to the aluminides on the aluminum-rich end where x is small. This relation derives from Eq. (11) by making a simple Taylor-series expansion about $x=0$, noting that in typical cases $d\Omega_A/dx \ll \Omega_A$ for small x, and then using Eq. (12):

$$\Omega_0=[1-(1-Z_B^0/Z_A^0)x]\Omega_A^0, \tag{16}$$

TABLE I. Valences and atomic volumes for the $3d$ aluminides TM_xAl_{1-x} in the $x=1$ and $x=0$ concentration limits, with volumes in a.u. For Al, $Z_A=3$ at all x and $\Omega_A=112.0$ a.u. at $x=0$. At $x=1$, $Z=Z_B$ and $\Omega=\Omega_B$; at $x=0$, $Z=Z_A$ and $\Omega=\Omega_A$. For conversion of volumes to Å^3 units, $\Omega(\text{Å}^3)=0.148\,18\ \Omega(\text{a.u.})$.

	$x=1$			$x=0$	
TM	Z_B	Ω_B	Ω_A	Z_B	Ω_B
Sc	1.616	168.7	313.2	2.190	81.74
Ti	1.515	119.2	236.0	2.408	89.87
V	1.424	93.23	196.4	2.339	87.34
Cr	1.410	80.94	172.3	2.196	81.99
Mn	1.482	83.16	168.3	2.047	76.42
Fe	1.472	79.47	162.0	1.912	71.34
Co	1.461	75.10	154.2	1.800	67.19
Ni	1.484	73.82	149.3	1.733	64.69
Cu	1.651	79.68	144.8	1.805	67.37

where Z_B^0 is Z_B evaluated at $x=0$, $Z_A^0=3$, and $\Omega_A^0=112.0$ a.u. (16.60 Å^3), the observed equilibrium volume of Al. Physically, this result is, apart from the replacement of Z_B with Z_B^0, equivalent to the condition of constant electron density Z/Ω, as was suggested by Phillips *et al.*[3] as an appropriate criterion for Co-Al phases. Equation (16) can be applied more generally, however, and is sometimes useful in the range $x<0.30$.

Finally, it should be pointed out that while our description of the zeroth-order electron density in TM compounds and alloys is internally consistent, any definition of a transition-metal valence Z_B in a condensed-matter system is method dependent and consequently not entirely unique. In fact, this subject has historically been approached in a rather different way for many aluminum-rich TM aluminides. These systems have often been treated as classic Hume-Rothery alloys whose stability is presumed to arise from the interaction of a set of dominant Bragg reflection planes with a nearly-free-electron Fermi surface. In this context, an effective transition-metal valence Z_B^{eff} can be defined, in our notation, as

$$Z_B^{\text{eff}}x=Z^{\text{eff}}-Z_A(1-x), \tag{17}$$

where $Z^{\text{eff}}=(k_F^{\text{eff}})^3\Omega_0/3\pi^2$ is the number of valence electrons contained within a free-electron Fermi sphere of radius k_F^{eff} just touching the Bragg planes in question. Thus k_F^{eff} is equated to $K/2$, which is one-half the magnitude of the reciprocal lattice vector defining these planes. This approach has been developed by Raynor[21] and by others. It leads to the interesting prediction of negative values for Z_B^{eff}, typically in the range -1 to -3, and thus to the concept of a negative effective TM valence in these alloys. The apparent contradiction between such *large and negative* values of Z_B^{eff} and our *large and positive* values of Z_B can be readily explained, however. For this one must take into account the important role of the TM d states on the electronic structure of these systems. This role has recently been discussed by Trambly de Laissardière *et al.*[8] on the basis of LDA calculations, which are, in fact, commensurate with our GPT treatment, as demonstrated in Sec. IV below. These studies confirm that there is a substantial contribution to the electronic structure from the TM d states and, in particular, near the Fermi level sp-d hybridization contributes to the formation of more complex pseudogaps in the density of states than envisaged in a simple Hume-Rothery model. This has the effect of blurring the meaning of Z^{eff} in Eq. (17), so that there is no precise quantitative relationship between k_F^{eff} and K. Qualitatively at least, Friedel[22] has argued that $k_F^{\text{eff}}>K/2$, which is significant because at small x, Z_B^{eff} is clearly very sensitive to k_F^{eff}. For example, at $x=0.2$ an increase of less than 10% in k_F^{eff} is needed to increase Z_B^{eff} by $+4$. Moreover, there is no theoretical or experimental evidence for the large transfer of electrons from sp states to TM d states implied by a large negative TM valence, although as pointed out by Trambly de Laissardière *et al.* there are extra sp states induced below the Fermi level by sp-d hybridization that could accommodate the transfer. At the same time, the presence of such states further indicates that Z^{eff} in Eq. (17) is not accounting for the entire sp valence population, as is the case in the definitions

of Z and Z_B in the GPT. Consequently, one fully expects $Z>Z^{\rm eff}$ and, depending on the value of $k_F^{\rm eff}$ chosen, either $Z_B>Z_B^{\rm eff}$ or $Z_B\gg Z_B^{\rm eff}$.

III. GPT INTERATOMIC POTENTIALS

The real-space total-energy functional of a general AB intermetallic system can be written

$$E_{\rm tot}(\mathbf{R}_1,\ldots,\mathbf{R}_N)=NE_{\rm vol}(\Omega,x)+\frac{1}{2}\sum_{\alpha,\beta=A,B}\sum_{i,j}{}'\,v_2^{\alpha\beta}(R_{ij};\Omega,x)+\cdots, \tag{18}$$

where by symmetry $v_2^{BA}=v_2^{AB}$ in the two-ion contributions and the ellipsis represents three- and four-ion contributions that are generalized similarly. Here it is understood that $R_{ij}=|\mathbf{R}_i\{\alpha\}-\mathbf{R}_j\{\beta\}|$, so that the sums over i and j are only over sites occupied by the atomic species α and β, respectively. In this section we discuss the specific forms the volume term $E_{\rm vol}$ and interatomic potentials $v_2^{\alpha\beta}$, etc., assume when A is a simple metal and B is a transition metal.

The volume term $E_{\rm vol}$ is most readily expressed as a series of contributions that are explicitly linear or quadratic in the concentration variables c_A and c_B:

$$\begin{aligned}E_{\rm vol}&=c_AE_1^A+c_BE_1^B+c_A^2E_2^{AA}+c_Ac_BE_2^{AB}+c_B^2E_2^{BB}+\delta E_{\rm vol}\\&=(1-x)E_1^A+xE_1^B+(1-x)^2E_2^{AA}+(1-x)xE_2^{AB}\\&\quad+x^2E_2^{BB}+\delta E_{\rm vol},\end{aligned} \tag{19}$$

where all energies E_1^α and $E_2^{\alpha\beta}$, with $\alpha,\beta=A$ or B, retain a volume dependence and an additional implicit concentration dependence and $\delta E_{\rm vol}$ is a small residual contribution with a more complex concentration dependence. Each linear component E_1^α may be further broken down into a large pseudoatom cohesive-energy contribution $E_{\rm coh}^{{\rm pa},\alpha}$, as introduced for the elemental metal in Ref. 12, and a smaller band-structure contribution δE_1^α:

$$E_1^\alpha=E_{\rm coh}^{{\rm pa},\alpha}+\delta E_1^\alpha. \tag{20}$$

For the simple-metal A component,

$$E_{\rm coh}^{{\rm pa},A}=E_{\rm fe}^A+\frac{2\Omega}{(2\pi)^3}\int_{k<k_F}w_{\rm pa}^A(\mathbf{k})d\mathbf{k}-E_{\rm bind}^{{\rm atom},A}(Z_A), \tag{21}$$

while for the transition-metal B component,

$$\begin{aligned}E_{\rm coh}^{{\rm pa},B}&=E_{\rm fe}^B+E_{\rm vol}^d+\frac{2\Omega}{(2\pi)^3}\int_{k<k_F}w_{\rm pa}^B(\mathbf{k})d\mathbf{k}-E_{\rm bind}^{{\rm atom},B}(Z_B)\\&\quad+E_{\rm prep}.\end{aligned} \tag{22}$$

Here $E_{\rm fe}^\alpha$ is the free-electron energy of component α,

$$E_{\rm fe}^\alpha=\frac{3}{5}Z_\alpha\epsilon_F+Z_\alpha\epsilon_{\rm xc}-\frac{3}{5}(Z_\alpha e)^2/R_{\rm WS}^\alpha+ZV_0', \tag{23}$$

where $\epsilon_{\rm xc}$ is the exchange and correlation energy of the free-electron gas, $R_{\rm WS}^\alpha$ is the Wigner-Seitz radius corresponding to the atomic volume Ω_α [i.e., $\Omega_\alpha=4\pi(R_{\rm WS}^\alpha)^3/3$], and V_0' is a constant that determines the zero of energy. The quantity $w_{\rm pa}^\alpha(\mathbf{k})$ is an appropriate plane-wave pseudopotential matrix element for component α, as defined in the Appendix, and $E_{\rm vol}^d$ is the transition-metal d-state contribution

$$E_{\rm vol}^d=Z_d^B(\epsilon_F-E_d^{{\rm vol},B})-\frac{10}{\pi}\int_0^{\epsilon_F}\delta_2(E)dE, \tag{24}$$

where $E_d^{{\rm vol},B}$ is the volume component of the B-metal d-state energy E_d^B, which denotes the position of the d bands in the alloy. The quantity $E_{\rm bind}^{{\rm atom},\alpha}(Z_\alpha)$ is the binding energy of the Z_α s and p valence electrons in the free atom, while $E_{\rm prep}$ is the preparation energy required to take the transition-metal free atom from its ground state to the same configuration employed in the alloy with valence Z_B. The remaining band-structure energies δE_1^α in Eq. (20) and $E_2^{\alpha\beta}$ and $\delta E_{\rm vol}$ in Eq. (19) arise mostly from higher-order pseudopotential and hybridization contributions and are discussed in the Appendix. As was demonstrated in Ref. 12, $E_{\rm coh}^{{\rm pa},B}$ alone already provides a good description of the equilibrium cohesive energy of pure transition metals in the $x=1$ limit. This is somewhat less true, however, of $E_{\rm coh}^{{\rm pa},A}$ for polyvalent simple metals such as Al, where δE_1^A and E_2^{AA} together contribute about one-third of the cohesive energy in the $x=0$ limit. In general, one needs full calculations of $E_{\rm tot}$, including both the volume and structural contributions, to adequately describe the cohesive energy, equilibrium volume, and heat of formation in TM_xAl_{1-x} compounds and alloys.

The AA or simple-metal pair potential has the familiar form of a screened Coulomb potential

$$v_2^{AA}(r;\Omega,x)=\frac{(Z_A^*e)^2}{r}\left[1-\frac{2}{\pi}\int_0^\infty F_N^{AA}(q;\Omega,x)\frac{\sin(qr)}{q}dq\right], \tag{25}$$

where Z_A^* is an effective valence and F_N^{AA} is a normalized energy-wave-number characteristic that embodies detailed electronic band-structure effects in the alloy including the self-consistent electron screening. The quantity F_N^{AA} is given by

$$F_N^{AA}(q;\Omega,x)=-\frac{q^2\Omega}{2\pi(Z_A^*e)^2}F_{ss}^{AA}(q;\Omega,x), \tag{26}$$

where, in the general case,

$$\begin{aligned}F_{ss}^{\alpha\beta}(q;\Omega,x)&=\frac{2\Omega}{(2\pi)^3}\int_{k<k_F}\frac{w^\alpha(\mathbf{k},\mathbf{q})w^\beta(\mathbf{k},\mathbf{q})}{\epsilon_{\mathbf{k}}-\epsilon_{\mathbf{k}+\mathbf{q}}}d\mathbf{k}\\&\quad-\frac{2\pi e^2\Omega}{q^2}\{[1-G(q)]n_{\rm scr}^\alpha(q)n_{\rm scr}^\beta(q)\\&\quad+G(q)n_{\rm OH}^\alpha(q)n_{\rm OH}^\beta(q)\},\end{aligned} \tag{27}$$

with $\alpha=\beta=A$ in Eq. (26). Here the quantities

$$w^\alpha(\mathbf{k},\mathbf{q})\equiv\langle\mathbf{k}+\mathbf{q}|w^\alpha|\mathbf{k}\rangle \tag{28}$$

are plane-wave matrix elements of the self-consistently screened atomic pseudopotential for component α. The quantity $G(q)$ is the exchange-correlation functional defined

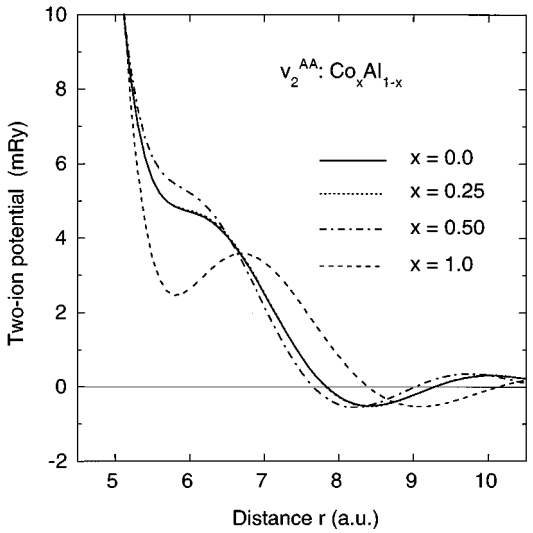

FIG. 3. The Al-Al pair potential v_2^{AA} in Co_xAl_{1-x} at four values of concentration x. In each case, the potential is evaluated at the observed or estimated equilibrium atomic volume Ω_0.

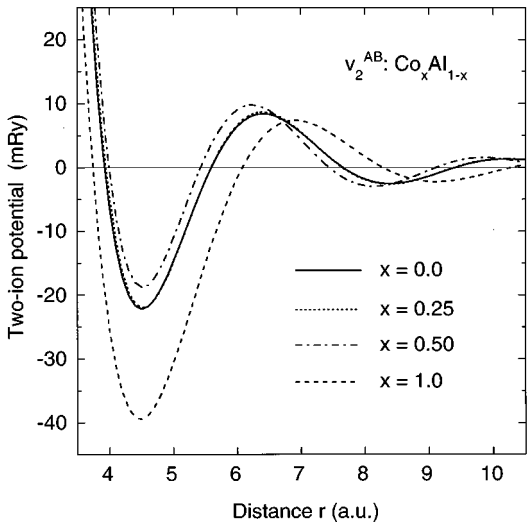

FIG. 4. The Co-Al pair potential v_2^{AB} in Co_xAl_{1-x} under the same conditions as in Fig. 3.

in Ref. 10. As in Ref. 12, we use the analytic expression for $G(q)$ developed by Ichimaru and Itsumi,[23] except that G is now referenced to the exchange-correlation energy of Vosko, *et al.*[19] rather than that of Hedin and Lundqvist[20] as done previously. The quantities $n_{\rm scr}^{\alpha}$ and $n_{\rm oh}^{\alpha}$ are screening and orthogonalization-hole contributions to the electron density from component α. In real space, the orthogonalization-hole density $n_{\rm oh}^{\alpha}$ represents a depletion of electron density from the core region of each α site. The corresponding effective valence Z_{α}^{*} is defined to exactly compensate this depletion:

$$Z_{\alpha}^{*}=Z_{\alpha}-\int n_{\rm oh}^{\alpha}(\mathbf{r})d\mathbf{r}, \tag{29}$$

with $\alpha=A$ in Eqs. (25) and (26). Additional technical details concerning the above equations are given in the Appendix.

The behavior of v_2^{AA} is illustrated in Fig. 3 for Co_xAl_{1-x} at various concentrations x. In each case the potential has been evaluated at either the observed or estimated equilibrium volume Ω_0. At $x=0$, v_2^{AA} is the pair potential for pure elemental Al. This result displays the characteristic features of a repulsive shoulder at near-neighbor distances and an oscillatory structure beginning at intermediate distances, which become the usual Friedel oscillations at long range. For $x=0.25$, the potential is almost unchanged and this reflects the near constancy of the electron density Z/Ω_0 for small x. Even for $x=0.5$ the potential is only modestly affected, with a slightly more repulsive shoulder and contracted oscillations reflecting a somewhat higher electron density. At $x=1$, however, the repulsive shoulder has developed into a clear local minimum in the potential and the oscillatory field has been pushed out to larger distances. This behavior is a direct consequence of the large atomic volume Ω_A that Al is forced to assume in this limit, as was discussed above.

The AB pair potential between the simple- and transition-metal components has the form

$$v_2^{AB}(r;\Omega,x)=\frac{Z_A^{*}Z_B^{*}e^2}{r}\left[1-\frac{2}{\pi}\int_0^{\infty}F_N^{AB}(q;\Omega,x)\frac{\sin(qr)}{q}dq\right], \tag{30}$$

where F_N^{AB} is given by

$$F_N^{AB}(q;\Omega,x)=-\frac{q^2\Omega}{2\pi Z_A^{*}Z_B^{*}e^2}[F_{ss}^{AB}(q;\Omega,x)+F_{sd}^{AB}(q;\Omega,x)], \tag{31}$$

with F_{ss}^{AB} given by Eq. (27) for $\alpha=A$ and $\beta=B$ and with

$$F_{sd}^{AB}(q;\Omega,x)=\frac{2\Omega}{(2\pi)^3}\int\frac{w^A(\mathbf{k},\mathbf{q})h_{11}^B(\mathbf{k},\mathbf{q})}{\epsilon_{\mathbf{k}}-\epsilon_{\mathbf{k}+\mathbf{q}}}d\mathbf{k}. \tag{32}$$

The quantity h_{11}^B represents a direct sp-d hybridization interaction that is given in the Appendix. This contribution, plus the indirect hybridization contributions through $n_{\rm scr}^B$ and $n_{\rm oh}^B$, have a large impact on the shape and magnitude of the pair potential v_2^{AB}. This is illustrated in Fig. 4, where v_2^{AB} for Co_xAl_{1-x} is plotted at the same concentrations x as in Fig. 3. The characteristic features of v_2^{AB} are a large attractive potential well near 4.5 a.u. (2.4 Å) and a long-range oscillatory structure that is in phase with but of larger magnitude than that of v_2^{AA}. The concentration dependence of v_2^{AB} is also very similar to that of v_2^{AA}, with very little effect on the potential for small x, but a deepening of the potential well and an expansion of the oscillatory field at $x=1$.

Finally, the BB or transition-metal pair potential has the form

$$v_2^{BB}(r;\Omega,x)=\frac{(Z_B^{*}e)^2}{r}\left[1-\frac{2}{\pi}\int_0^{\infty}F_N^{BB}(q;\Omega,x)\frac{\sin(qr)}{q}dq\right]+v_{\rm ol}^{BB}(r;\Omega,x), \tag{33}$$

where F_N^{BB} is given by

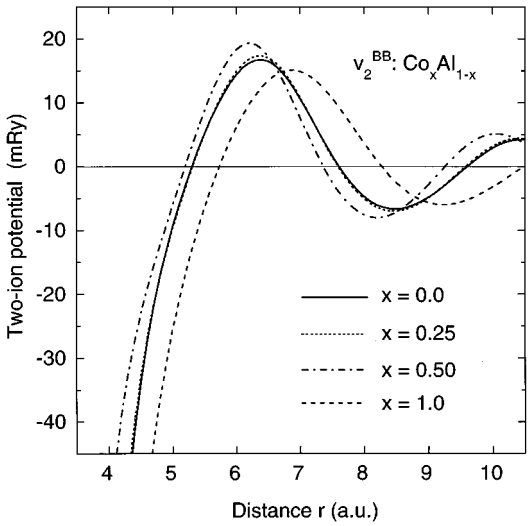

FIG. 5. The Co-Co pair potential v_2^{BB} in Co_xAl_{1-x} under the same conditions as in Fig. 3.

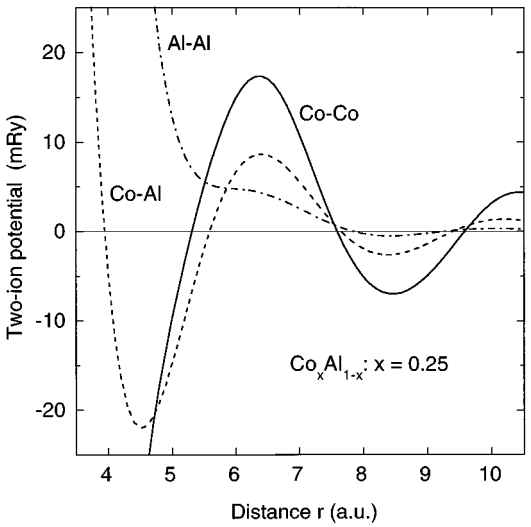

FIG. 6. The Al-Al potential v_2^{AA}, the Co-Al potential v_2^{AB}, and the Co-Co potential v_2^{BB} for Co_xAl_{1-x} at a concentration $x=0.25$.

$$F_N^{BB}(q;\Omega,x)=-\frac{q^2\Omega}{2\pi(Z_B^*e)^2}[F_{ss}^{BB}(q;\Omega,x)+2F_{sd}^{BB}(q;\Omega,x)+F_{dd}^{BB}(q;\Omega,x)], \tag{34}$$

with F_{ss}^{AB} given by Eq. (27) for $\alpha=\beta=B$, F_{sd}^{BB} given by Eq. (32) with A replaced by B, and

$$F_{dd}^{BB}(q;\Omega,x)=\frac{2\Omega}{(2\pi)^3}\int\frac{h_{21}^B(\mathbf{k},\mathbf{q})}{\epsilon_{\mathbf{k}}-\epsilon_{\mathbf{k}+\mathbf{q}}}d\mathbf{k}. \tag{35}$$

Here h_{21}^B represents a second, related sp-d hybridization interaction that is also defined in the Appendix. The potential v_2^{BB} has the same formal structure as the result for pure transition metals. The additional overlap potential $v_{\rm ol}^{BB}$ contains all direct d-d interactions between ions and is given by Eq. (142) of Ref. 12. The d-state band-structure component of $v_{\rm ol}^{BB}$ has the form

$$v_2^{d,BB}(R_{ij};\Omega,x)$$
$$=\frac{2}{\pi}\,\mathrm{Im}\int_0^{\epsilon_F}\ln[\det(I-T_{ij}T_{ji})]dE$$
$$=-\frac{2}{\pi}\,\mathrm{Im}\int_0^{\epsilon_F}\mathrm{Tr}[T_{ij}T_{ji}+\tfrac{1}{2}(T_{ij}T_{ji})^2+\cdots]dE, \tag{36}$$

where T_{ij} is the energy dependent, 5×5 d-state matrix that couples sites i and j, as defined in Eq. (90) of Ref. 12. This component embodies a significant bonding contribution arising from the partially filled d bands and leads to a strongly attractive pair potential v_2^{BB} at short range, as illustrated in Fig. 5 for Co_xAl_{1-x}. Although a very deep potential well develops in v_2^{BB} below 4 a.u. (2.1 Å) for Co_xAl_{1-x} and other central-transition-metal systems (e.g., see Fig. 14 of Ref. 12), this well is not actually physically accessible. At small x, TM near-neighbor distances are sufficiently large so as to avoid the short-ranged part of v_2^{BB} entirely, while at larger x, the attractive well of v_2^{BB} is compensated for by repulsive multi-ion interactions at short range arising from v_3^{BBB} and v_4^{BBBB}. At longer range, v_2^{BB} develops a qualitatively similar oscillatory structure to v_2^{AB} but with larger-amplitude oscillations. The concentration dependence of v_2^{BB} is also very similar to that of both v_2^{AB} and v_2^{AA}.

The v_2^{AA} Al-Al, v_2^{AB} Co-Al, and v_2^{BB} Co-Co potentials are compared at $x=0.25$ in Fig. 6. The increase in energy scale in going from v_2^{AA} to v_2^{AB} to v_2^{BB} is typical of the central transition metals. The variation of v_2^{BB} with atomic number in the pure $3d$ transition metals is illustrated in Fig. 14 of Ref. 12. At the ends of the series in Sc and Ni, v_2^{BB} at short range is substantially reduced in magnitude and becomes comparable to v_2^{AB}, while in the extreme limit of Cu all three potentials are reduced to the same energy scale as v_2^{AA}. At the same time, the first minimum in v_2^{BB} for Sc, Ni, and Cu also moves outward to the vicinity of a bulk nearest-neighbor distance and in Cu_xAl_{1-x} the first minimum in both v_2^{AB} and v_2^{BB} is raised to positive energy, as shown in Fig. 7 at $x=0$. The variation of v_2^{AB} with atomic number in the $3d$ alu-

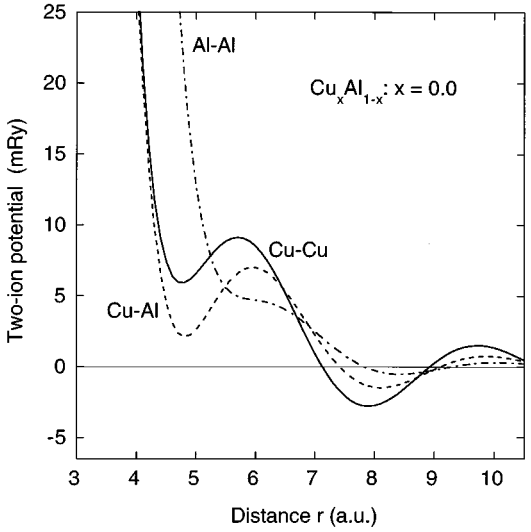

FIG. 7. The Al-Al potential v_2^{AA}, the Cu-Al potential v_2^{AB}, and the Cu-Cu potential v_2^{BB} for Cu_xAl_{1-x} in the dilute alloy $x=0$ limit.

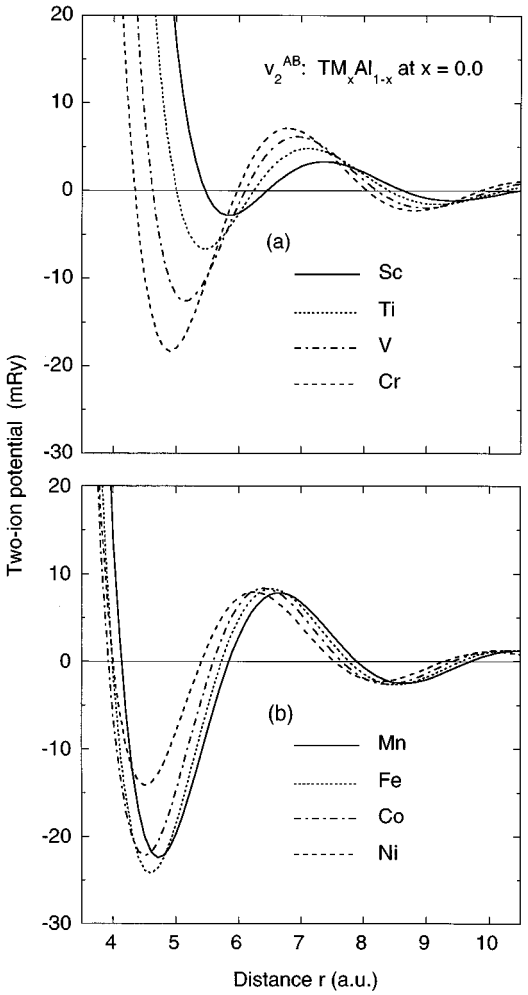

FIG. 8. The TM-Al potential v_2^{AB} across the $3d$ series for TM_xAl_{1-x} aluminides in the dilute alloy $x=0$ limit. (a) Sc, Ti, V, and Cr; (b) Mn, Fe, Co, and Ni.

minides from Sc to Ni is illustrated in Fig. 8 at $x=0$. Note that the position of the first minimum in this potential steadily decreases in distance across the series from about 5.8 a.u. (3.1 Å) in Sc to about 4.5 a.u. (2.4 Å) in Ni. This clear trend has important structural consequences for small-x compounds and alloys, as we will discuss in Sec. IV.

As with the transition-metal pair potential v_2^{BB}, the multi-ion potentials v_3^{BBB} and v_4^{BBBB} have identical formal structure to those in the pure metal. These latter potentials are dominated by their d-state components and are approximated in the GPT by the multi-ion generalizations of $v_2^{d,BB}$, as given by Eqs. (106) and (107) of Ref. 12. In the applications discussed below, v_3^{BBB} is calculated in the form

$$v_3^{BBB}(R_{ij},R_{jk},R_{ki};\Omega,x)=\frac{2}{\pi}\,\mathrm{Im}\int_0^{\epsilon_F}\mathrm{Tr}[T_{ij}T_{jk}T_{ki}+T_{ik}T_{kj}T_{ji}-(T_{ij}T_{ji}T_{ik}T_{ki}+T_{jk}T_{kj}T_{ji}T_{ij}+T_{ki}T_{ik}T_{kj}T_{jk})]dE, \quad (37)$$

which is truncated at fourth order in the T_{ij}. The behavior of v_3^{BBB} across the $3d$ series for the pure transition metals is illustrated in Fig. 18 of Ref. 12. This behavior is made complex by the sp-d hybridization, which introduces significant oscillatory structure into the potential. For the separations $R_{ij}=R_{jk}=1.8R_{WS}$ shown in the figure, v_3^{BBB} is largely repulsive for the central transitions metals but attractive for Sc and for the late members of the series. At somewhat shorter separations, where the direct d-d interactions dominate, v_3^{BBB} tends to become more repulsive in nature, especially for the central transition metals.

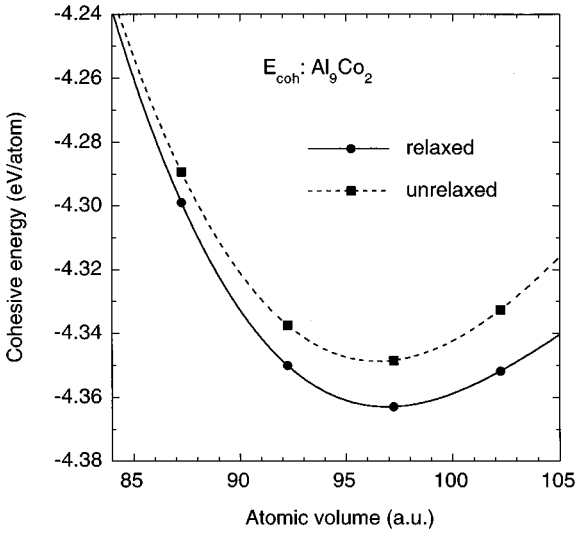

FIG. 9. Volume dependence of the cohesive energy E_{coh} for monoclinic Al_9Co_2 obtained both with and without relaxation of its 22-atom unit cell. Symbols represent calculated points, while the solid and dashed lines are analytic fits to these results.

IV. TRENDS IN COHESION AND STRUCTURE

In this section we consider a few illustrative applications of the above GPT formalism to the problems of cohesion and structure in the $3d$ aluminides. Our primary intent here is to demonstrate the expected capabilities and promise of the theory in these areas. We plan to provide more extensive tests of the Co-Al and Ni-Al pair potentials elsewhere, where the structural phase diagrams of these materials will be considered in detail.

At the pair potential level, the present theory can provide reliable estimates of the cohesive properties of transition-metal aluminides for concentrations $x<0.30$. We expect such calculations, in fact, to be similar in quality to full LDA electronic-structure results. At the same time, the simplified GPT total-energy functional (18) permits one to consider complex structures without difficulty, including the full relaxation of all internal coordinates. We illustrate these capabilities here by considering the cohesive properties of Al_9Co_2 in its observed monoclinic phase with 22 atoms per primative unit cell and corresponding to $x=0.1818$. In Fig. 9 we have plotted the volume dependence of the cohesive energy, $E_{coh}=E_{tot}/N$ both with and without relaxation of all atomic positions in the unit cell. Relaxation, which is accomplished through a conjugate-gradient method to be described elsewhere, lowers the energy by about 0.01–0.02 eV/atom near equilibrium. In calculating the pair-potential contributions to E_{coh} in Eq. (18), we have dealt with the long-range Friedel

TABLE II. Cohesive properties of monoclinic Al_9Co_2 with 22 atoms per unit cell.

	LMTO-ASA[a] unrelaxed	GPT unrelaxed	GPT relaxed	Experiment
$\lvert E_{\rm coh}\rvert$ (eV)		4.35	4.36	3.95[b]
ΔH (eV)	−0.46	−0.31	−0.32	−0.31[c]
$\Omega_{\rm eq}$ (a.u.)	96.2	96.5	96.9	102.2[d]
B (Mbar)	1.08	1.19	1.05	

[a]Reference 8.
[b]Inferred from measured values of ΔH, $E_{\rm coh}^{\rm Co}$, and $E_{\rm coh}^{\rm Al}$ via Eq. (38).
[c]Reference 24.
[d]Reference 25.

tails of the potentials $v_2^{\alpha\beta}$ by everywhere imposing a cutoff at a distance of $8.25R_{\rm WS}$, where $R_{\rm WS}$ is the Wigner-Seitz radius corresponding to the atomic volume Ω [i.e., $\Omega=4\pi R_{\rm WS}^3/3$]. This procedure provides adequate convergence and a smooth volume dependence to $E_{\rm coh}$. The same procedure has also been used in all remaining calculations discussed below, except as noted.

The calculated equilibrium cohesive properties of Al_9Co_2 are tabulated in Table II and compared with experiment[24–26] and also with previous LDA calculations obtained from the linear muffin-tin orbital (LMTO) method in the atomic-sphere approximation (ASA) for the observed (unrelaxed) structure.[8] Listed are the cohesive energy $E_{\rm coh}$; the heat of formation ΔH, as calculated from $E_{\rm coh}$ and the cohesive energies of Co and Al via the relation

$$\Delta H = E_{\rm coh} - xE_{\rm coh}^{\rm Co} - (1-x)E_{\rm coh}^{\rm Al}; \tag{38}$$

the equilibrium atomic volume $\Omega_{\rm eq}$; and the bulk modulus B. The agreement between theory and experiment is good, and for the fully relaxed GPT calculations, the equilibrium volume is obtained to within about 5% of the observed value. The very close agreement obtained for the heat of formation ΔH, on the other hand, may be somewhat fortuitous. This quantity depends significantly on the value of the transition-metal cohesive energy $E_{\rm coh}^{\rm Co}$ used for pure Co in Eq. (38). We have calculated this quantity at the pair-potential level, as done for the other contributions, but this leads to an overestimate of its magnitude. We expect that the net effect of the neglected multi-ion contributions would be to lower the magnitude of $E_{\rm coh}^{\rm Co}$ and consequently raise the magnitude of ΔH. This expectation is also consistent with the larger magnitude of ΔH obtained in the LMTO-ASA calculations.

We have also examined the cohesive and structural trends across the $3d$ series in the special case of the transition-metal trialuminides Al_3TM corresponding to $x=0.25$. These results are plotted in Figs. 10 and 11. Here we have considered five candidate structures: cubic $L1_2$ with four atoms per primative unit cell, tetragonal $D0_{22}$ with four atoms per cell and an ideal c/a ratio of 2.0, cubic $D0_3$ with four atoms per cell, cubic A_{15} with eight atoms per cell, and orthorhombic $D0_{11}$ with 16 atoms per cell. Among these five structures, the predicted structural sequence across the $3d$ series is $L1_2 \rightarrow D0_{22} \rightarrow D0_{11}$ and the lowest-energy structure in each case has been used to calculate the cohesive energy $E_{\rm coh}$ in Fig. 10. The predicted sequence of structures is generally

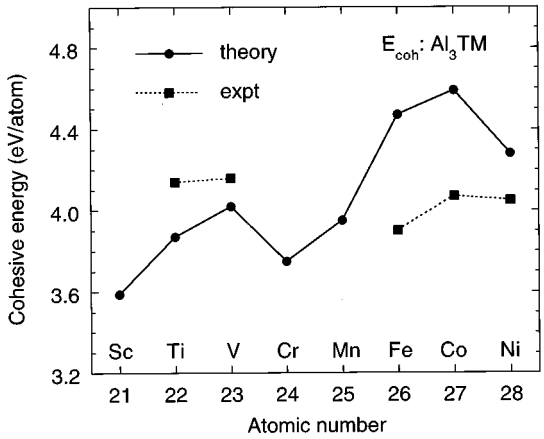

FIG. 10. Trends in the cohesive energy of $3d$ transition-metal trialuminides Al_3TM corresponding to $x=0.25$. The theoretical results refer to the lowest-energy structures displayed in Fig. 11, while the experimental results derive from the measured heats of formation and the cohesive energies of the elemental metals.

commensurate with what is observed in Al_3TM compounds: Al_3Sc is $L1_2$, Al_3Ti and Al_3V are $D0_{22}$, although with non-ideal c/a ratios, and Al_3Ni is $D0_{11}$. In the cases of Al_3Cr and Al_3Mn trialuminides do not form, while in the cases of Al_3Fe and Al_3Co more complex, nonstoichiometric structures are found near $x=0.25$. As will be shown elsewhere, $D0_{11}$ is indeed energetically competitive with these latter structures. The predicted cohesive energies show a more modest variation across the $3d$ series with values in the range 3.6–4.6 eV for all of the trialuminides. For the five systems where experimental heat-of-formation data exist, the inferred cohesive energies [via Eq. (38) with $E_{\rm coh}^{\rm Co}$ replaced by $E_{\rm coh}^{\rm TM}$] are all near 4.0 eV.

The structural trends illustrated in Fig. 11 for the $3d$ trialuminides can be understood in terms of the contributions from the individual interatomic potentials. In particular, we have investigated in detail the subtle competition between the $L1_2$ and $D0_{22}$ structures for the early members of the

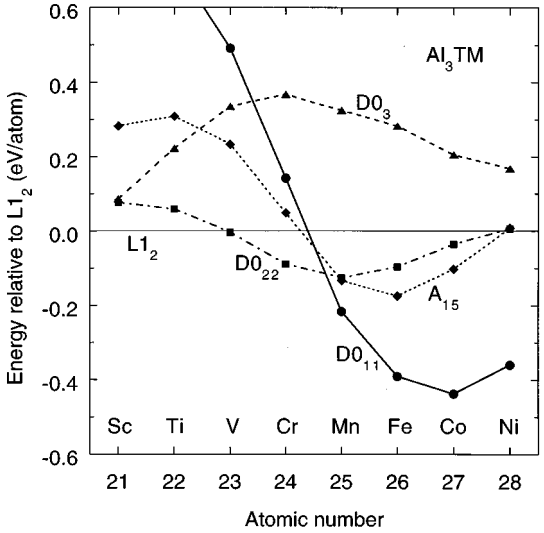

FIG. 11. Calculated structural trends among five candidate structures in the $3d$ transition-metal trialuminides Al_3TM, corresponding to $x=0.25$.

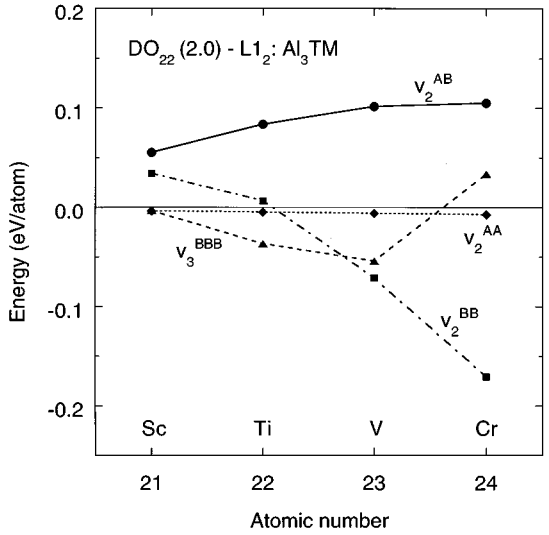

FIG. 12. Two- and three-ion potential contributions to the $D0_{22}$-$L1_2$ energy difference for the early $3d$ transition-metal trialuminides, Al_3TM. Here $c/a=2.0$ for the $D0_{22}$ structure.

series[27] and also the overall competition between the close-packed $L1_2$ and $D0_{22}$ structures and the open-packed $D0_{11}$ structure. Figure 12 displays both the v_2^{AA}, v_2^{AB}, and v_2^{BB} two-ion potential contributions included in Fig. 11 and also the additional v_3^{BBB} three-ion contribution to the $D0_{22}-L1_2$ energy difference for the first four $3d$ trialuminides, with $c/a=2.0$ for the $D0_{22}$ structure as above. At the pair potential level, it is seen that the transition-metal potential v_2^{BB} drives the calculated $L1_2\rightarrow D0_{22}$ trend shown in Fig. 11, while v_2^{AA} has little effect and v_2^{AB} opposes the trend, favoring the $L1_2$ structure for all the trialuminides. The effect of the three-ion transition-metal potential v_3^{BBB} is to favor the $D0_{22}$ structure in Al_3Ti and Al_3V but the $L1_2$ structure in Al_3Cr. The sum of all four calculated contributions is displayed in Fig. 13 and compared with the LDA band theory calculations of Carlsson and Meschter[4] for Al_3Sc, Al_3Ti, and Al_3V. There is quantitative agreement for Al_3Ti, but the magnitude of the $L1_2\rightarrow D0_{22}$ trend is apparently underesti-

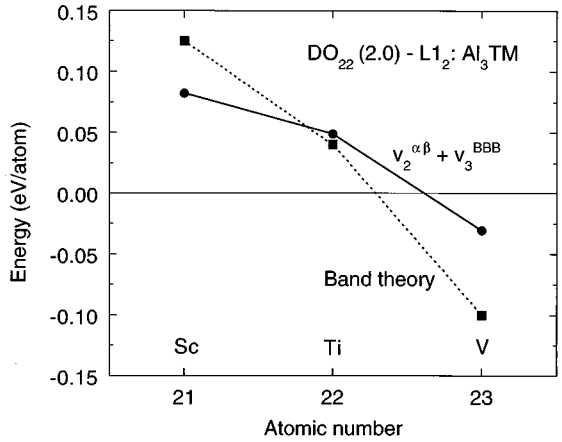

FIG. 13. Calculated $D0_{22}$-$L1_2$ energy difference, with $c/a=2.0$ in the $D0_{22}$ structure, for Al_3Sc, Al_3Ti, and Al_3V, as obtained from the present GPT interatomic potentials and from the band-theory results of Ref. 4. Here $v_2^{\alpha\beta}$ denotes the sum of v_2^{AA}, v_2^{AB}, and v_2^{BB}.

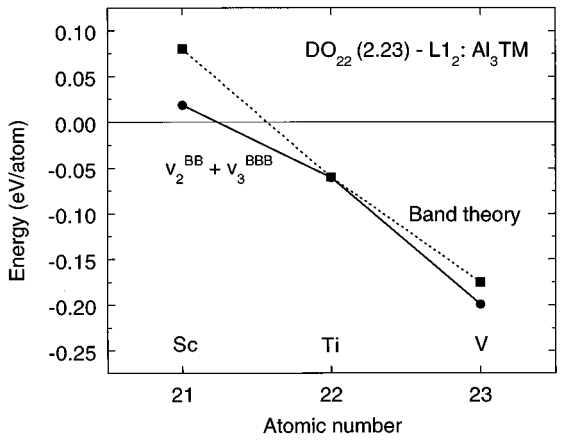

FIG. 14. Calculated $D0_{22}$-$L1_2$ energy difference, with $c/a=2.23$ in the $D0_{22}$ structure, for Al_3Sc, Al_3Ti, and Al_3V, as obtained from the present GPT interatomic potentials $v_2^{BB}+v_3^{BBB}$ and from the band-theory results of Ref. 4.

mated with the GPT potentials, so that additional, neglected multi-ion contributions may be of importance here as well.

Experimentally, both Al_3Ti and Al_3V are observed to form in a $D0_{22}$ structure with a higher than ideal c/a axial ratio near 2.23. This distortion is necessary, in fact, to make the $D0_{22}$-$L1_2$ energy difference negative in the case of Al_3Ti, as shown by the LDA calculations of Carlsson and Meschter.[4] The real-space explanation of a high c/a ratio in terms of the GPT interatomic potentials is a more subtle matter, however. The transition-metal potentials v_2^{BB} and v_3^{BBB} both favor this distortion, but v_2^{AA} and v_2^{AB} oppose it, and they do so to the extent that the observed $D0_{22}$ structure is not explained at this level of description. Nonetheless, it is very interesting to note that if one considers only the v_2^{BB} and v_3^{BBB} contributions to the $D0_{22}$-$L1_2$ energy difference with $c/a=2.23$, one obtains both the correct trend in the early trialuminides and quantitative agreement with the LDA band-theory results for Al_3Ti and Al_3V, as shown in Fig. 14. This suggests that the unfavorable contributions from v_2^{AA} and v_2^{AB} may be largely canceled by neglected higher-order potential contributions from v_3^{AAB}, v_3^{ABB}, etc. It remains to be seen, however, whether or not this cancellation can actually be demonstrated in practice.

While the $L1_2\rightarrow D0_{22}$ trend in the early trialuminides is driven by transition-metal interactions through v_2^{BB} and v_3^{BBB}, it is the pair potential v_2^{AB} that is largely responsible for the overall trend of relatively close-packed $L1_2$ and $D0_{22}$ structures at the beginning of the $3d$ series and more open-packed structures such as $D0_{11}$ towards the end of the series. In particular, the appearance of the $D0_{11}$ structure is highly correlated with the movement of the first deep potential minimum in v_2^{AB} (see Fig. 8) from a position $r_{\min}>1.7R_{\mathrm{WS}}$ for the first four members of the series to a position $r_{\min}<1.7R_{\mathrm{WS}}$ for the last four members. This is quantified in Fig. 15. As shown in that figure, the AB nearest neighbors for the ideal $D0_{22}$ structure are located at $1.81R_{\mathrm{WS}}$ while the nearest neighbors for the observed $D0_{11}$ structure are clustered near $1.6R_{\mathrm{WS}}$. For convenience, the values of $r_{\min}$ displayed in Fig. 15 are actually those obtained from the $x=0$

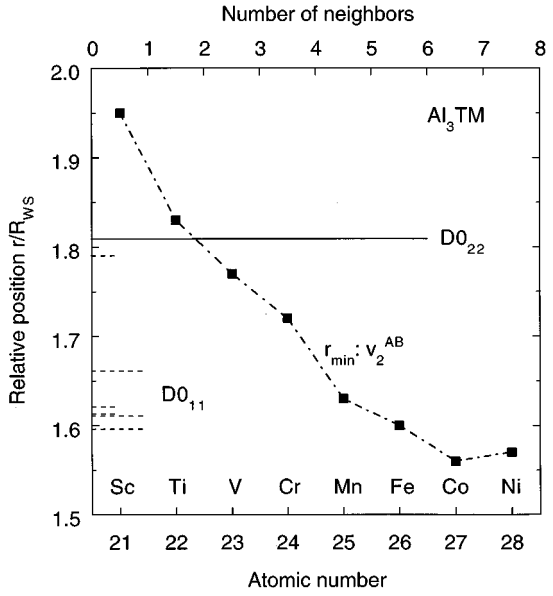

FIG. 15. Origin of the relative stability of the $D0_{22}$ and $D0_{11}$ structures across the $3d$ transition-metal trialuminides Al_3TM. Plotted are (i) the position of the first minimum $r_{\min}$ in the potential v_2^{AB} (solid points), referred to the lower horizontal scale, and (ii) the number and position of the AB nearest neighbors for the $D0_{22}$ (solid line) and $D0_{11}$ (dashed lines) structures, referred to the upper horizontal scale. Positions are in units of $R_{\rm WS}$.

potentials shown in Fig. 8; the values for the $x=0.25$ potentials should not be substantially different.

V. CONCLUSIONS

We have achieved in this paper a first-principles generalized pseudopotential theory of interatomic potentials for sp-d-bonded AB intermetallic compounds and alloys where A is a simple metal and B is a transition metal. The theory explicitly provides for an *ab initio* LDA treatment of the volume term $E_{\rm vol}$, the central-force pair potentials v_2^{AA}, v_2^{AB}, and v_2^{BB}, and the angular-force multi-ion potentials v_3^{BBB} and v_4^{BBBB} in the total-energy functional, including the full volume and concentration dependence of all quantities. Successful application of the formalism has been made to the aluminum-rich transition-metal aluminides where the volume term and pair potentials dominate the energetics. At the pair-potential level of description, the cohesive and structural properties are mostly well described for $x<0.30$, although some structural subtleties may require multi-ion contributions for a proper explanation, as appears to be the case with the distorted $D0_{22}$ structure occurring in the early trialuminides. More generally, we expect the present GPT pair potentials to be applicable to static and dynamic simulations of structural, thermodynamic, and mechanical properties of complex systems, both ordered and disordered. This includes nonstoichiometric solid phases with 100 or more atoms and 10% or more vacancies in the unit cell, as occur in the Co-Al phase diagram. We shall explicitly treat such phases elsewhere.

Further extensions of the present GPT formalism are also possible. One implicit extension, which is already treated by our computer codes but has not been discussed here, is to the case where the B component is either a series-end transition metal (e.g., Ca or Zn), with an empty or filled d band, or another simple metal (e.g., Mg). Such systems can be well treated at the pair-potential level for all concentrations x. More difficult extensions are to high-concentration transition-metal aluminides and to d-bonded systems where the A component is also a transition metal. In general, such systems will require a direct account of the additional v_3^{AAB}, v_3^{ABB}, etc. multi-ion interactions, which have not been been treated here. With regard to the aluminides, important special cases include TiAl, NiAl, and Ni_3Al. In some of these systems, it may be possible to fold down the multi-ion interactions into effective pair contributions that can be added to v_2^{AB} and v_2^{BB}.

ACKNOWLEDGMENTS

The work of J.A.M. was performed under the auspices of the U.S. Department of Energy by the Lawrence Livermore National Laboratory under Contract No. W-7405-ENG-48. M.W. acknowledges support by the National Science Foundation under Grant No. DMR-9221596.

APPENDIX

In this appendix we elaborate additional technical details about the GPT formalism for binary intermetallic systems. We begin with the A- and B-component zeroth-order pseudoatoms and the determination of the zero-of-energy constant V_0', which couples the two pseudoatoms. The construction of the α-component pseudoatom and the self-consistent potential $v_{\rm pa}^{\alpha}$ and related quantities defining it are formally the same as for the pure metal. In particular, Eqs. (79)–(82) of Ref. 12 are the principal defining equations for the transition-metal B component. Within this basic pseudoatom scheme, the only variable quantity is the logarithmic derivative D_2^*, which serves as a boundary condition on the localized d states ϕ_d^B. In all applications discussed here, we utilize the nominal choice $D_2^*=-3$, which identifies $E_d^{{\rm vol},B}$ as the center of the d bands.

To determine V_0' we first define an average pseudopotential $w_{\rm pa}$ with diagonal plane-wave matrix elements

$$\langle \mathbf{k}|w_{\rm pa}|\mathbf{k}\rangle = c_A\langle \mathbf{k}|w_{\rm pa}^A|\mathbf{k}\rangle + c_B\langle \mathbf{k}|w_{\rm pa}^B|\mathbf{k}\rangle, \tag{A1}$$

where the A- and B-component pseudopotentials are given by

$$\langle \mathbf{k}|w_{\rm pa}^{\alpha}|\mathbf{k}\rangle = \langle \mathbf{k}|v_{\rm pa}^{\alpha}|\mathbf{k}\rangle - V_0' + \sum_c\ (\epsilon_{\mathbf{k}} - E_c^{{\rm vol},\alpha})\langle \mathbf{k}|\phi_c^{\alpha}\rangle\langle \phi_c^{\alpha}|\mathbf{k}\rangle, \tag{A2}$$

with $\alpha=A$ or B. The quantity ϕ_c^{α} is an α-component core state, while $E_c^{{\rm vol},\alpha}$ is the volume component of the corresponding core energy

$$E_c^{{\rm vol},\alpha} = E_c^{{\rm pa},\alpha} - \langle \phi_c^{\alpha}|\,\delta V_{\rm unif}|\,\phi_c^{\alpha}\rangle - V_0', \tag{A3}$$

where $E_c^{{\rm pa},\alpha}$ is the core eigenvalue of the α-component pseudoatom and the additional free-electron-gas potential $\delta V_{\rm unif}$ is defined in Ref. 12. The $\mathbf{k}=\mathbf{0}$ condition

$$\langle 0|w_{\rm pa}|0\rangle = 0 \tag{A4}$$

places the zero of energy at the bottom of the valence bands in the full intermetallic system. Using this condition in Eq. (A1) and solving for V_0' yields the result

$$V_0' = \frac{c_A\langle 0|w_{\rm pa}^A|0\rangle_0 + c_B\langle 0|w_{\rm pa}^B|0\rangle_0}{1 - c_A\langle 0|p_c^A|0\rangle - c_B\langle 0|p_c^B|0\rangle}, \tag{A5}$$

where p_c^α is the α-component core projection operator $\Sigma_c|\phi_c^\alpha\rangle\langle\phi_c^\alpha|$ and

$$\langle 0|w_{\rm pa}^\alpha|0\rangle_0 = \langle 0|w_{\rm pa}^\alpha|0\rangle + V_0'(1 - \langle 0|p_c^\alpha|0\rangle), \tag{A6}$$

in which the dependence on V_0' is removed from $\langle 0|w_{\rm pa}^\alpha|0\rangle$.

The simple-metal A pseudoatom is coupled to the transition-metal B pseudoatom only indirectly through its volume Ω_A and does not otherwise depend on the zero-of-energy constant V_0'. The B pseudoatom, on the other hand, is coupled to the A pseudoatom through both its volume Ω_B and its valence Z_B, which depend directly on V_0'. The latter dependence comes through Eqs. (13)–(15) via the phase shift δ_2 determining Z_d^B. Using Eqs. (63) and (65) of Ref. 12, δ_2 can be written directly in terms of the d-state energy $E_d^{{\rm vol},B}$ and hence V_0':

$$Z_d^B = -\frac{2}{\pi}\,{\rm Im}\sum_d \ln[\epsilon_F - E_d^{{\rm vol},B} - \Gamma_{dd}^{{\rm vol},B}(\epsilon_F)], \tag{A7}$$

where

$$E_d^{{\rm vol},B} = E_d^{{\rm pa},B} - \langle\phi_d^B|\,\delta V_{\rm unif}\,|\phi_d^B\rangle - V_0' \tag{A8}$$

and $\Gamma_{dd}^{{\rm vol},B}$ is the volume component of the d-state self-energy, as defined in Ref. 12. Consequently, an efficient strategy to calculate the A and B pseudoatoms self-consistently for a given volume Ω and concentration x is as follows

(i) Choose a trial value for Ω_A and calculate the A pseudoatom. This determines values for $\langle 0|w_{\rm pa}^A|0\rangle_0$ and $\langle 0|p_c^A|0\rangle$ entering Eq. (A5) for V_0'.

(ii) Evaluate Ω_B from Eq. (11) and calculate the B pseudoatom, assuming $Z/\Omega = Z_B/\Omega_B$ in Eq. (14). This determines values for V_0', Z_d^B, Z_B, and ϵ_F.

(iii) Iterate (i) and (ii) until the condition $Z_A/\Omega_A = Z_B/\Omega_B$ is satisfied. When this condition is satisfied, the assumption in (ii) is also exactly true.

We next turn to the intermetallic total energy and the various contributions to the volume term $E_{\rm vol}$ and pair potentials $v_2^{\alpha,\beta}$ defined in Eqs. (19)–(35). In Eqs. (21) and (22) for $E_{\rm coh}^{{\rm pa},\alpha}$ we employ the notation

$$w_{\rm pa}^\alpha(\mathbf{k}) \equiv \langle\mathbf{k}|w_{\rm pa}^\alpha|\mathbf{k}\rangle \tag{A9}$$

for $\alpha = A$ and B. In the equations below we similarly write $w_{\rm pa}(\mathbf{k}) \equiv \langle\mathbf{k}|w_{\rm pa}|\mathbf{k}\rangle$ and

$$p_c^\alpha(\mathbf{k}) \equiv \langle\mathbf{k}|p_c^\alpha|\mathbf{k}\rangle. \tag{A10}$$

We also define the general sp-d hybridization interaction

$$h_{nm}^B(\mathbf{k},\mathbf{q}) = -\frac{1}{\pi}\,{\rm Im}\int_0^{\epsilon_F} \frac{\left[\sum_d v'_{\mathbf{k}+\mathbf{q}d} v'_{d\mathbf{k}}\right]^n}{(E - E_r^B)^n (E - \epsilon_{\mathbf{k}})^m} dE, \tag{A11}$$

where n and m are integers and E_r^B is the complex and energy dependent d-state resonance position

$$E_r^B = E_d^{{\rm vol},B} + \Gamma_{dd}^{{\rm vol},B}(E). \tag{A12}$$

The terms $v'_{\mathbf{k}+\mathbf{q}d}$ and $v'_{d\mathbf{k}}$ can be expressed in terms of plane-wave d-state nonorthogonality and hybridization matrix elements. For example,

$$v'_{\mathbf{k}d} = -(E - E_d^{{\rm vol},B})\langle\mathbf{k}|\phi_d^B\rangle - \langle\mathbf{k}|\Delta_{\rm vol}|\phi_d^B\rangle, \tag{A13}$$

where $\Delta_{\rm vol}$ is the volume component of the d-state hybridization potential Δ defined in Ref. 12. The choice $n = m = 1$ in Eq. (A11) gives h_{11}^B appearing in Eq. (32) for F_{sd}^{AB}, while the choice $n = 2$, $m = 1$ gives h_{21}^B appearing in Eq. (35) for F_{dd}^{BB}.

Using the above quantities, one can write out the remaining components of $E_{\rm vol}$ defined in Eqs. (19) and (20). First, δE_1^α takes the form

$$\delta E_1^A = E_{\rm oh}^A + \frac{1}{2}(Z_A^* e)^2\left[\frac{1.8}{R_{\rm WS}^A} - \frac{2}{\pi}\int_0^\infty F_N^{AA}(q;\Omega,x)\,dq\right] \tag{A14}$$

for the simple-metal A component and

$$\delta E_1^B = E_{\rm oh}^B + \frac{1}{2}(Z_B^* e)^2\left[\frac{1.8}{R_{\rm WS}^B} - \frac{2}{\pi}\int_0^\infty F_N^{BB}(q;\Omega,x)\,dq\right] + \frac{1}{\pi}{\rm Im}\int_0^{\epsilon_F}\sum_d \frac{[\Gamma_{dd}^{{\rm vol},B}(E)]^2}{(E - E_r^B)^2} dE \tag{A15}$$

for the transition-metal B component. Here $E_{\rm oh}^\alpha$ for $\alpha = A$ or B is the self-energy of the orthogonalization hole, as defined in Eq. (50) of Ref. 11. The additional energies $E_2^{\alpha,\beta}$ are given by the expressions

$$E_2^{AA} = \frac{2\Omega}{(2\pi)^3}\int_{k<k_F} p_c^A(\mathbf{k}) w_{\rm pa}^A(\mathbf{k})\,d\mathbf{k} + (Z_A^* e)^2\frac{\pi}{\Omega}\frac{\partial^2 F_N^{AA}(0;\Omega,x)}{\partial q^2}, \tag{A16}$$

$$E_2^{AB} = \frac{2\Omega}{(2\pi)^3}\int_{k<k_F}[p_c^A(\mathbf{k}) w_{\rm pa}^B(\mathbf{k}) + w_{\rm pa}^A(\mathbf{k}) p_c^B(\mathbf{k})]\,d\mathbf{k} + \frac{2\Omega}{(2\pi)^3}\int[w_{\rm pa}^A(\mathbf{k}) h_{12}^B(\mathbf{k},0) + p_c^A(\mathbf{k}) h_{11}^B(\mathbf{k},0)]\,d\mathbf{k} + (Z_A^* Z_B^* e^2)\frac{2\pi}{\Omega}\frac{\partial^2 F_N^{AB}(0;\Omega,x)}{\partial q^2}, \tag{A17}$$

and

$$E_2^{BB}=\frac{2\Omega}{(2\pi)^3}\int_{k<k_F} p_c^B(\mathbf{k})w_{\rm pa}^B(\mathbf{k})d\mathbf{k} + \frac{2\Omega}{(2\pi)^3}\int [w_{\rm pa}^B(\mathbf{k})h_{12}^B(\mathbf{k},0)+p_c^B(\mathbf{k})h_{11}^B(\mathbf{k},0) + \tfrac{1}{2}h_{22}^B(\mathbf{k},0)]d\mathbf{k}+(Z_B^* e)^2\frac{\pi}{\Omega}\frac{\partial^2 F_N^{BB}(0;\Omega,x)}{\partial q^2}. \tag{A18}$$

The final correction term in Eq. (19) can be expressed as

$$\delta E_{\rm vol}=-\frac{1}{2}w_{\rm pa}(\mathbf{k}_F)\,\delta Z_{\rm band}, \tag{A19}$$

where

$$\delta Z_{\rm band}=w_{\rm pa}(\mathbf{k}_F)\frac{c_B\rho_0(\epsilon_F)\rho_d(\epsilon_F)}{\rho_0(\epsilon_F)+c_B\rho_d(\epsilon_F)}, \tag{A20}$$

with $\rho_0(\epsilon_F)$ and $\rho_d(\epsilon_F)$ the free-electron and d-state densities of states at the Fermi level, respectively.

Finally, we discuss the screening and orthogonalization-hole components of the valence electron density, which directly enter Eq. (27) for $F_{ss}^{\alpha,\beta}$. The simple-metal, A-component screening density can be written

$$n_{\rm scr}^A(q)=\frac{4}{(2\pi)^3}\int_{k<k_F}\frac{w^A(\mathbf{k},\mathbf{q})}{\epsilon_{\mathbf{k}}-\epsilon_{\mathbf{k}+\mathbf{q}}}d\mathbf{k}, \tag{A21}$$

while the transition-metal, B-component screening density is given by

$$n_{\rm scr}^B(q)=\frac{4}{(2\pi)^3}\int_{k<k_F}\frac{w^B(\mathbf{k},\mathbf{q})}{\epsilon_{\mathbf{k}}-\epsilon_{\mathbf{k}+\mathbf{q}}}d\mathbf{k}+\frac{4}{(2\pi)^3}\int\frac{h_{11}^B(\mathbf{k},\mathbf{q})}{\epsilon_{\mathbf{k}}-\epsilon_{\mathbf{k}+\mathbf{q}}}d\mathbf{k}. \tag{A22}$$

In these equations $w^\alpha(\mathbf{k},\mathbf{q})$ is the matrix element

$$\langle\mathbf{k}+\mathbf{q}|w^\alpha|\mathbf{k}\rangle=\langle\mathbf{k}+\mathbf{q}|v^\alpha|\mathbf{k}\rangle+\sum_c(\epsilon_{\mathbf{k}}-E_c^{{\rm vol},\alpha})\langle\mathbf{k}+\mathbf{q}|\phi_c^\alpha\rangle \times\langle\phi_c^\alpha|\mathbf{k}\rangle \tag{A23}$$

for $\alpha=A$ or B. Here v^A and v^B are the A- and B-component self-consistent atomic potentials, which in turn depend on $n_{\rm scr}^A$ and $n_{\rm scr}^B$, respectively. In each case, one can use the generalized Poisson equation (38) of Ref. 11 to express v^α in terms of $n_{\rm scr}^\alpha$ and thereby eliminate v^α and solve for $n_{\rm scr}^\alpha$ self-consistently. The simple-metal, A-component orthogonalization-hole density contains only inner-core contributions arising from p_c^A and can be calculated from Eq. (132) of Ref. 12. The transition-metal, B-component orthogonalization-hole density has both inner-core contributions from p_c^B and sp-d hybridization contributions from $v'_{\mathbf{k}d}$ and can be calculated from Eq. (131) of Ref. 12.

[1] J. Hafner, *From Hamiltonians to Phase Diagrams* (Springer-Verlag, Berlin, 1987), and references therein.

[2] J. Zou and A. E. Carlsson, Phys. Rev. B **47**, 2961 (1993); Phys. Rev. Lett. **70**, 3748 (1993); Phys. Rev. B **50**, 99 (1994).

[3] R. Phillips, J. Zou, A. E. Carlsson, and M. Widom, Phys. Rev. B **49**, 9322 (1994).

[4] A. E. Carlsson and P. J. Meschter, J. Mater. Res. **4**, 1060 (1989); **5**, 2813 (1990).

[5] A. E. Carlsson, Phys. Rev. B **43**, 12 176 (1991).

[6] M. A. Asta, D. de Fontaine, and M. van Schilfgaarde, J. Mater. Res. **8**, 2554 (1993).

[7] S. Öğüt and K. M. Rabe, Phys. Rev. B **50**, 2075 (1994).

[8] G. Trambly de Laissardière, D. Nguyen Manh, L. Magaud, J. P. Julien, F. Cyrot-Lackmann, and D. Mayou, Phys. Rev. B **52**, 7920 (1995); G. Trambly de Laissardière, D. Mayou, and D. Nguyen Manh, Europhys. Lett. **21**, 25 (1993).

[9] W. Kohn and L. J. Sham, Phys. Rev. **140**, A1133 (1965).

[10] J. A. Moriarty, Phys. Rev. B **16**, 2537 (1977).

[11] J. A. Moriarty, Phys. Rev. B **26**, 1754 (1982).

[12] J. A. Moriarty, Phys. Rev. B **38**, 3199 (1988).

[13] M. J. Mehl, J. E. Osburn, D. A. Papaconstantopoulos, and B. M. Klein, Phys. Rev. B **41**, 10 311 (1990).

[14] C. L. Fu, Y.-Y. Ye, M. H. Yoo, and K. M. Ho, Phys. Rev. B **48**, 6712 (1993).

[15] S. M. Foiles and M. S. Daw, J. Mater. Res. **2**, 5 (1987).

[16] A. F. Voter and S. P. Chen, Mater. Res. Soc. Symp. Proc. **82**, 175 (1987); S. P. Chen, D. J. Srolovitz, and A. F. Voter, J. Mater. Res. **4**, 62 (1989); S. P. Chen, Mater. Sci. Eng. B **6**, 113 (1990).

[17] S. I. Rao, C. Woodward, and T. A. Parthasarathy, Mater. Res. Soc. Symp. Proc. **213**, 125 (1991); J. P. Simmons, S. I. Rao, and D. M. Dimiduk, *ibid.* **288**, 335 (1993); T. A. Parthasarathy, S. I. Rao, and D. M. Dimiduk, Philos. Mag. A **67**, 643 (1993).

[18] L. Do Phuong, D. Nguyen Manh, and A. Pasturel, Phys. Rev. Lett. **71**, 372 (1993).

[19] S. H. Vosko, L. Wilk, and M. Nusair, Can. J. Phys. **58**, 1200 (1980).

[20] L. Hedin and B. I. Lundqvist, J. Phys. C **4**, 2064 (1971).

[21] G. V. Raynor, Prog. Met. Phys. **1**, 1 (1949).

[22] J. Friedel, Helv. Phys. Acta **61**, 538 (1988).

[23] S. Ichimaru and K. Utsumi, Phys. Rev. B **24**, 7385 (1981).

[24] F. R. de Boer, R. Boom, W. C. M. Mattens, A. R. Miedema, and A. K. Niessen, *Cohesion in Metals: Transition Metal Alloys* (Elsevier, Amsterdam, 1988), p. 273.

[25] P. Villars and L. D. Calvert, *Pearson's Handbook of Crystallographic Data for Intermetallic Phases* (American Society for Metals, Materials Park, OH, 1991), Vol. 1, p. 717.

[26] C. Kittel, *Introduction to Solid State Physics*, 5th ed. (Wiley, New York, 1976), p. 74.

[27] The GPT results shown in Figs. 12–14 have all been obtained with a potential cutoff of $10.30R_{\rm WS}$ rather than the standard $8.25R_{\rm WS}$ used elsewhere. This is necessary to ensure a reasonable level of convergence for the three-ion potential contribution from v_3^{BBB}. For v_3^{BBB}, the cutoff is applied separately to each of the three radial arguments of the potential function.